

# Comparative Optical Analysis of Imprinted Nano-, Micro- and Biotextures on Solar Glasses for Increased Energy Yield

Danbi Yoo, Peter Tillmann, Tobias Kraus, Johannes Sutter, Angelika Harter, Sergei Trofimov, Boris Naydenov, Klaus Jäger, Hubert Hauser, and Christiane Becker\*

In modern photovoltaic (PV) systems such as bifacial and building-integrated PV, a big share of sunlight impinges at large incident angles on the air-to-glass module interface. These designs exceedingly call for effective omnidirectional antireflective (AR) measures. Texturing of PV cover glasses can effectively mitigate reflection losses in a broad spectral and angular range. Numerous individual textures have been presented in the literature; however, the lack of consistent material stacks hinders a comparative evaluation. Herein, UV-nanoimprint lithography is used to fabricate and analyze 12 different artificial and bioreplicated textures from nano- to mesoscale on glass. The angle-resolved reflectance is examined for incident angles from 5° to 80° and analyzed the scattering properties. For example, the effect of the investigated textures on the annual energy yield is calculated for a tilted bifacial PV module located in Berlin, Germany. While well-known moth-eye nanostructures exhibit excellent AR behavior near-normal incidence, their shallow angle performance is often not reported. The best-performing textures exhibit features on microscale and a large surface enhancement factor, increasing the annual energy yield up to 5% when compared to nontextured devices. The results give clear design guidelines for textured glasses of future PV applications.

## 1. Introduction

Antireflective (AR) measures at the air-glass interface of photovoltaic (PV) modules are critical for optimizing power conversion efficiency (PCE), which is one of the most effective levers for lowering the levelized cost of PV energy. Ideally, reflection is suppressed over an extended spectral range, indifferent to polarizations and angles of incidence.<sup>[1]</sup> Antireflective coatings can be found in the vast majority of PV modules nowadays.<sup>[2]</sup> Single-layer antireflective (AR) coatings derived from sol-gel have been shown to reduce the front side reflection of glass from 4% to below 2% (broadband) at normal incidence.<sup>[3]</sup> The use of multilayer systems can improve AR performance even further, potentially resulting in reflection levels of less than 1% across a limited range of wavelengths.<sup>[4]</sup> For antireflective measures to be effective in PV applications, they must be able to capture solar radiation from all directions (omnidirectional) and for a wide

spectrum of light. Additionally, it is beneficial for these coatings to scatter light to increase the amount of light absorbed by the absorber material of solar cells, while also improving the appearance of PV modules by reducing glare and concealing the PV cells behind a diffuse cover glass. The importance of these characteristics is growing as PV technology is increasingly being implemented in urban areas and incorporated into buildings.

Texturing the air-glass interface of solar panels is a viable technique for achieving omnidirectional, broadband AR and light scattering. In the literature, AR textures with feature sizes varying from subwavelength to mesoscale dimensions are discussed. One can find a variety of studies on textured solar glasses, each of which focuses on either one particular texture or a particular group of textures. These textures include subwavelength-size nanotextures,<sup>[5,6]</sup> microtextures adapting random pyramids, which can be obtained through wet-chemical etching of silicon wafers, and implementing these textures on glass,<sup>[7,8]</sup> biomimetic textures from petals or leaves<sup>[9–10]</sup> and mesoscale textures.<sup>[11–13]</sup> Due to the diverse range of materials and solar cell stacks investigated in the previously reviewed publications, it is

D. Yoo, P. Tillmann, J. Sutter, A. Harter, S. Trofimov, B. Naydenov, K. Jäger, C. Becker

Division Solar Energy  
Helmholtz-Zentrum Berlin für Materialien und Energie  
12489 Berlin, Germany  
E-mail: christiane.becker@helmholtz-berlin.de

P. Tillmann, K. Jäger  
Computational Nano Optics  
Zuse Institute Berlin  
14195 Berlin, Germany

T. Kraus, H. Hauser  
Holotools  
Temicon GmbH  
79115 Freiburg, Germany

 The ORCID identification number(s) for the author(s) of this article can be found under <https://doi.org/10.1002/solr.202300071>.

© 2023 The Authors. Solar RRL published by Wiley-VCH GmbH. This is an open access article under the terms of the Creative Commons Attribution License, which permits use, distribution and reproduction in any medium, provided the original work is properly cited.

DOI: 10.1002/solr.202300071

challenging to compare the omnidirectional antireflective properties of the various AR textures. To the best of our knowledge, a comprehensive comparison of these various proposed AR textures inside a controlled testing environment has not yet been carried out. In addition, despite the fact that a wide range of AR textures has been researched, the evaluated angular range of angle-dependent optical characteristics varies largely, particularly incidence angles greater than 60° not being provided consistently. Reflectance data are frequently only supplied for normal incidence, even though that realistic illumination encompasses a broad angular range. However, because a significant portion of the light will be incident at large oblique angles, particularly in the context of developing PV concepts such as vertically installed PV, bifacial PV, and building integrated PV (BIPV), broadband, omnidirectional AR measures are becoming increasingly important.

In this work, we present 12 different AR textures from the nano-, micro-, and mesoregime, including artificial as well as bioreplicated textures, which are fabricated by UV-nanoimprint lithography (UV-NIL) on resist-coated glass substrates. The aim of this study is to sharpen the understanding of the potential impact of different structure types on the energy yield under realistic irradiance conditions. Angle-resolved reflectance is selected as a key classification parameter to assess the degree of omnidirectionality. Further, the angle-resolved scattering properties are investigated. We carefully study the structural parameters and their correlation to the angle-dependent optical properties. Finally, experimental angle-resolved reflectance data are implemented to estimate the energy yield of a bifacial module with textured glass tilted at 37° and facing south. For this, we use meteorological data for Berlin, Germany, and an in-house developed algorithm delivering the angular distribution of the incident light perceived by the module.

## 2. Results

We used UV-NIL to fabricate 12 different antireflective textures from the meso-, micro-, and nanoscale, including bioreplicated structures. **Figure 1** schematically shows the replication process of such a texture with UV-NIL. Each texture is initially carried by a master structure (Figure 1a). The master structure can either be manmade or based on a natural template. For the UV-NIL process, first, the viscoelastic polymer polydimethylsiloxane (PDMS) is casted on the master structure (Figure 1b), and transitions to an elastic solid stamp after a thermal curing process. The stamp carries the original structure's negative (neg.) (Figure 1c). The PDMS stamp is then applied to a UV-curable resist, predeposited to a glass substrate and cured under UV illumination (Figure 1d). A final thermal curing process results in a replica of the master structure on the glass substrate (Figure 1e). After thermal curing, the resist has a refractive index of ( $n_{\text{resist},589\text{ nm}} = 1.517$ ), which is very close to the refractive index of the glass substrate ( $n_{\text{glass},589\text{ nm}} = 1.509$ ). This procedure allows us to investigate the different textures using an identical material system and hence to characterize the impact of geometrical structure properties independently. The nanoimprinted replicas are used for structural analysis and optical characterization. Two examples of structural parameters are illustrated in Figure 1f. More details on processing are provided in the Experimental Section.

### 2.1. Structural Analysis

We extracted texture profiles of replicas with either laser scanning profilometry or atomic force microscopy (AFM), depending on the texture size and with respect to the height resolution of the instrument. The mean peak-to-peak distance was used to evaluate the lateral feature size of the surface, while the mean

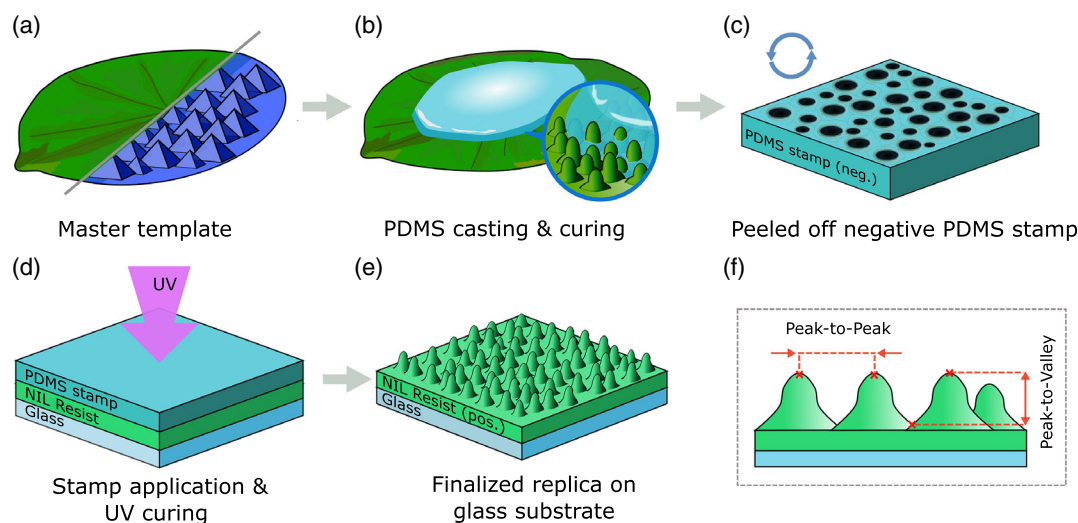


**Figure 1.** Processing steps for the replication of artificial and bio-inspired textures using UV-nanoimprint lithography. a) A master structure is either manufactured or a natural template is used. b) The surface textures are replicated by casting viscous PDMS to the master and thermal curing. c) The solidified viscoelastic PDMS stamp, carrying the negative (neg.) of the master structure is peeled off. d) The PDMS is applied to a UV-curable resist predeposited on a glass substrate and the resist is cured under UV exposure. e) The final replica is used for the structural and optical analysis. f) Illustrating lateral (peak-to-peak) and vertical (peak-to-valley) parameters, which are used to characterize the texture dimension. Partly adapted with permission.<sup>[21]</sup> Copyright 2021, IEEE.

peak-to-valley distance was used to quantify the vertical structural dimensions, as shown in Figure 1f. These parameters are considered to be more effective at visualizing the actual structural dimensions of individual elements than standard roughness quantities, such as arithmetic- and root-mean-square roughness, which describe the deviation in height from the mean line. Table S1, Supporting Information, lists the corresponding characterization method used for each texture and please note that both measurement setups were not calibrated to each other. The investigated textures and their structural parameters are summarized in **Table 1**. Selected scanning electron microscopy (SEM) images of representative investigated textures in **Figure 2** show the diversity of the sample pool, which we categorized into three classes: subwavelength-sized nanotextures, artificial microtextures, and biotextures. Please note that the frame color of each class used in Figure 2 is used for the entire document. The nanotextures shown in Figure 2a–c are outlined in red and consist of a moth-eye structure (by temicon GmbH<sup>[14]</sup>) with a surface covered in a fine array of protuberances (Figure 2a), a sinusoidal texture arranged in a hexagonal array (Figure 2b), both originally formed by laser interference lithography, and random nanopillars produced by wet-chemical etching with potassium hydroxide (KOH), potassium silicate (K<sub>2</sub>SiO<sub>3</sub>), and a commercial additive in silicon wafers (Figure 2c).<sup>[15]</sup> The feature sizes of these

nanotextures are found in the submicron range, with lateral dimensions ranging from 280 to 930 nm and vertical dimensions ranging from 70 to 310 nm. The artificial microtextures depicted in Figure 2d–f are outlined in blue and include hexagonally arranged microlens arrays (Figure 2d) produced by a combination of lithography and reflow processes, KOH-etched random micropillars in silicon (Figure 2e), and a stochastically textured wide-angle circular diffuser (by temicon GmbH<sup>[16]</sup>) specified with a scattering angle of 125° (FWHM) (Figure 2f). These microtextures have lateral dimensions ranging from 1.7 μm to 7.7 μm and peak-to-valley heights ranging from 2 to 6 μm. Since distinctively larger spreads in feature size are observed for certain textures of this class, please refer to the standard deviations provided in Table 1. The epidermal topographies of biotextures shown in Figure 2g–i, outlined in green, are derived from natural templates. The lotus leaf (*Nelumbo nucifera*) in Figure 2g has a surface texture characterized by microscale, protruding mound-like structures. The poinsettia leaf texture (*Euphorbia pulcherrima*) shown in Figure 2h is distinguished by smooth, dome-shaped features that are more densely packed with their adjacent neighbors compared to the previous lotus texture. The texture of the rose petal (Rosa) in Figure 2i is made up of even more closely packed, lens-shaped microscale papillae. Small-scale features known as “nanofolds” can be seen on top

**Table 1.** Summary of structural (gray) and optical (blue) properties of the textures investigated in this study. The ratio between diffuse and total transmittance is represented by the haze factor, while the directional transmittance, as used here, indicates the forward directional transmittance within the scattering angles of ±12.5°. Furthermore, minimum and maximum incident angle ( $\theta = 5^\circ, 80^\circ$ ) reflectances averaged over 330 to 830 nm are provided.

Texture	Scale	Peak-to-peak distance	Peak-to-valley distance	Surface enhancement factor	Haze avg. (330–1,200) nm [%]	Directional transmittance ± 12.5° [%]	Reflectance $\theta = 5^\circ$ [%]	Reflectance $\theta = 80^\circ$ [%]
Glass	–	–	–	1	0.1	99.9	4.4	36.7
Antireflection coating on glass (simulated)	–	–	–	–	–	–	4.4 <sup>c)</sup>	37.1 <sup>c)</sup>
Sinusoidal (hexagonal lattice)	Nano	(500 ± 11) nm	(199 ± 7) nm	1.2	0.8	99.3	1.5	37.5
Sinusoidal (square lattice)	Nano	(930 ± 34) nm	(95 ± 3) nm	1.1	6.8	94.6	4.3	37.4
Random nanopillars	Nano	(830 ± 360) nm	(313 ± 90) nm	1.4	37.9	89.8	2.2	24.8
Moth-eye structure	Nano	(365 ± 14) nm	(110 ± 6) nm	1.3	1.1	99.9	0.9	31.6
							1.7 <sup>c)</sup>	36.8 <sup>c)</sup>
Microlens array	Micro	(7.6 ± 0.1) μm	(4.4 ± 0.3) μm	2.5	99.9	11.7	1.3	11.9
Random micropillars	Micro	(1.9 ± 0.9) μm	(2.1 ± 0.1) μm	1.6	97.6	22.4	1.2	12.2
Diffuser (small angle)	Micro	(10.6 ± 3.7) μm	(1.6 ± 0.2) μm	1.3	76.1	92.3	4.5	24.5
Diffuser (wide angle)	Micro	(4 ± 1.2) μm <sup>a)</sup>	(2.4 ± 1.1) μm <sup>a)</sup>	4 <sup>a)</sup>	–	31.7	0.9	9.5
							0.9 <sup>c)</sup>	9.3 <sup>c)</sup>
Lotus leaf	Bio	(17.6 ± 6.4) μm	(14.3 ± 2.9) μm	>2.9 <sup>b)</sup>	94.8	53.7	3.4	9.5
Rose petal	Bio	(30.1 ± 4.4) μm	(15.5 ± 2.3) μm	>3.9 <sup>b)</sup>	99	7.1	1.1	7.0
							1.2 <sup>c)</sup>	6.5 <sup>c)</sup>
Poinsettia leaf	Bio	(29 ± 4.4) μm	(14.5 ± 3.6) μm	3.1	98.2	34.4	2.5	8.1
Commercial AR foil	Meso	–	–	–	99.8	8.6	0.6	10.2

<sup>a)</sup>Accurate surface parameters proved challenging to obtain, resulting in only approximate height information. <sup>b)</sup>The surface enhancement factor of biostructures was calculated only considering the larger microtexture. Submicron features were not considered leading to an underestimation of the real surface enhancement factor. <sup>c)</sup>The reflectance values are averaged over 420 to 1,150 nm for an accurate energy yield calculation.

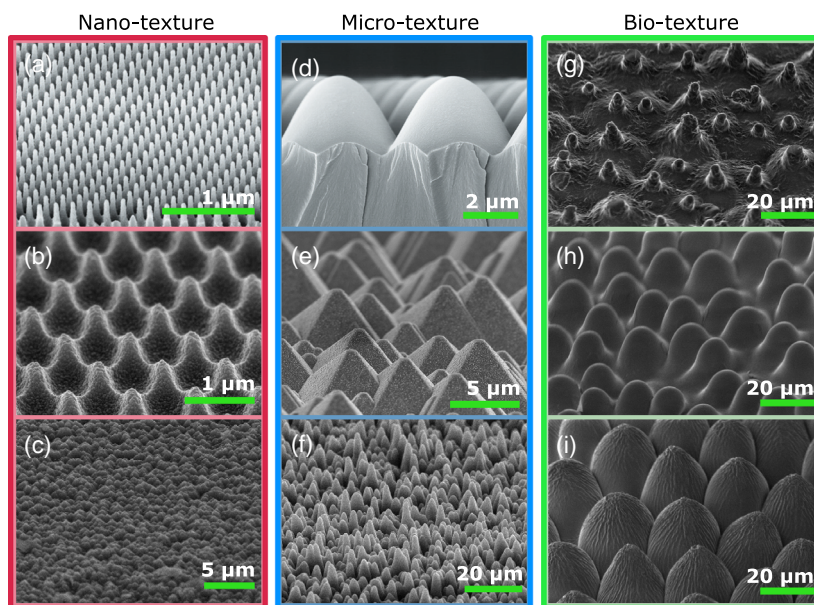


**Figure 2.** Scanning electron microscopy images of selected a–c) nanotextures (red), d–f) microtextures (blue), and g–i) replicated biotextures (green). The SEM images of the master structures are shown for the a) moth-eye structure (by temicon GmbH), b) sinusoidal (hexagonal lattice)—silver evaporated, c) random nanopyramids in silicon, d) microlens array (by temicon GmbH<sup>[14]</sup>), e) random micropyramids in silicon,<sup>[15]</sup> and f) wide-angle circular diffuser (by temicon GmbH<sup>[16]</sup>). SEM images of replicated structures in resist on glass are shown for g) lotus leaf, h) poinsettia leaf, and i) rose petal.

of the papillae.<sup>[17]</sup> Biotextures have microscale features, with lateral dimensions ranging from 17 to 30  $\mu\text{m}$  and depth dimensions ranging from 13 to 17  $\mu\text{m}$ , which are the largest structures among the samples. Although the dimensions of these textures are similar to those of the previous group of artificial microtextures, they are distinguished based on their different origins of the master structure. In addition to those textures shown in Figure 2, the analysis also included a sinusoidal square lattice nanotexture, a small angle Gaussian circular diffuser specified with a scattering angle of 15° (FWHM) (by temicon GmbH<sup>[16]</sup>), and the texture of a mesoscopic commercial AR texture.<sup>[13]</sup> The structural properties of the latter cannot be fully disclosed here. It serves as a performance reference for optical characterization.

In addition, we assessed characteristic surface area parameters with the peak density, which is the number of peaks per unit area ( $\text{mm}^{-2}$ ) (Table S1, Supporting Information). With increasing feature sizes, we observe a reduction of the peak density, as the texture elements scale up relative to the fixed unit area. The peak density magnitudes range from  $10^6 \text{mm}^{-2}$  for the smallest nanotextures,  $10^4$  to  $10^5 \text{mm}^{-2}$  for the microtextures, and reach magnitudes of  $10^3 \text{mm}^{-2}$  for the biostructures.

We further evaluated the surface enhancement factor (SEF), which is a measure of texture-induced surface area enlargement defined as the ratio of real surface area to the projection area in the horizontal plane. Consequently, it is calculated by dividing the scanned real surface area to its corresponding projected area. The SEF of a perfectly flat surface equals unity, while a texture doubling the surface area would correspond to a SEF value of 2. For convenience, the SEF of the planar glass substrates ( $R_{\text{RMS,Glass}} < 0.5 \text{ nm}$ ) was assumed to be unity. Parameters such as peak density and structure depth have a large impact on the SEF, as they determine structural elevation and the frequency of

irregularities. In our sample collection, nanotextures enhance the surface area by 20% to 40% ( $\text{SEF} = 1.2\text{--}1.4$ ), whereas the investigated microtextures exhibit surface enhancement between 30% and 400% ( $\text{SEF} = 1.3\text{--}4$ ). Please note that the surface parameter of the wide-angle diffuser proved challenging to obtain, resulting in only approximate height information. Despite this limitation, these measurements were included for completeness and to demonstrate the sample's exceptional optical performance, as noted in Table 1 accordingly. For biotextures, SEFs larger than 3 are observed. As shown in Figure 2i, a small-scale nanoscale surface roughness, previously described as nanocuticular folds, is well visible, and modulated on top of each microscale feature of the rose petal.<sup>[18]</sup> In contrast, nanocrystalloids, i.e., epicuticular waxes, covering the microscale features of the lotus leaf (Figure 2g) as described by Barthlott et al. are only visible on a few features in the replicated sample and with much lower density than reported.<sup>[19]</sup> A complete replication of the nanoscale waxes by UV-NIL was reported to be challenging.<sup>[20]</sup> However, we have previously reported that a certain degree of structural fidelity is sufficient to reproduce the widely known lotus effect with a suitable choice of the target material by means of UV-NIL.<sup>[21]</sup>

Nevertheless, the influence of the nanoscale textures is not included in the SEF, as they are beyond the z-axis resolution of the confocal laser scanning profilometer. Due to these characterization limitations, we report an underestimated SEF without the contribution of the nanotextures but expect an increased value, especially, for the rose texture, where the entirety of the hierarchical structure is fully replicated.

The high SEF of 3.9 for the rose texture may also arise from its packing efficiency, where each structural element is closely packed to its adjacent features as can be seen in Figure 2i. A densely packed structure translates into efficient utilization

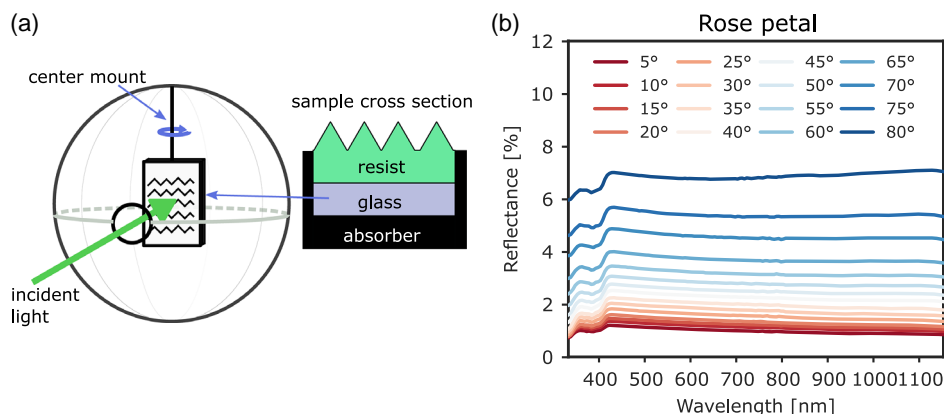
of the projection area, reducing the fraction of unoccupied surface area. In contrast, the poinsettia and lotus structures (Figure 2g,h) have both similar lateral and horizontal dimensions as the rose structure, but larger unoccupied spacings between neighboring features are visible. This effect is notably larger for the lotus than for the poinsettia structure, as suggested by the difference in SEF (Poinsettia: 3.1, Lotus: 2.9). The observed relationship of the SEF with the optical properties of the respective structures is elaborated in the following section.

## 2.2. Angle-Resolved Reflectance

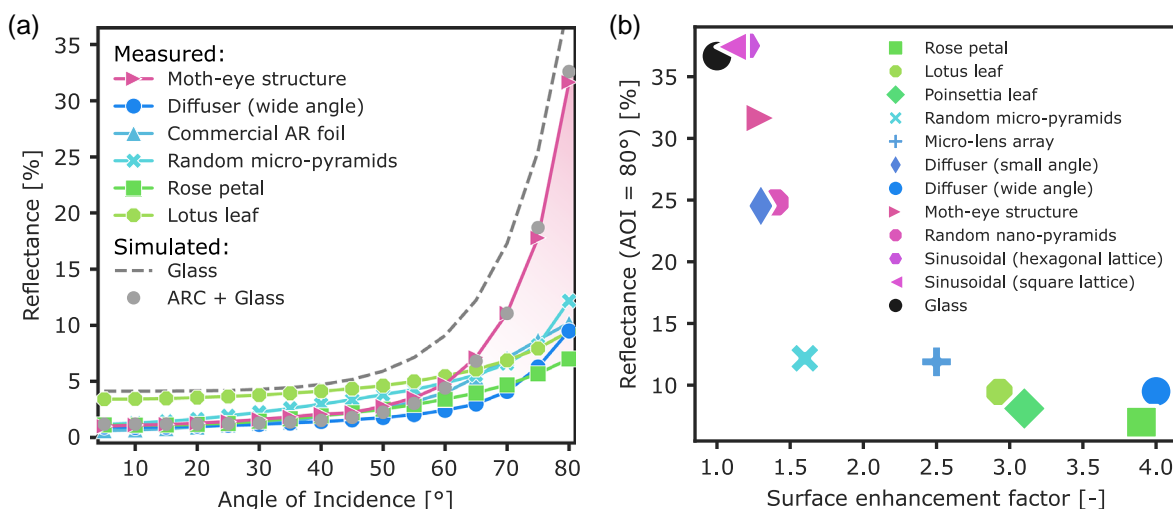
After the structural analysis was completed, the optical properties of the AR textures were assessed by means of reflectance analysis under varying incident angles to quantify the omnidirectional AR performance. A UV-vis-NIR spectrophotometer was used to measure the reflectance with varying incident angles as illustrated in Figure 3a, using a rotatable center mount sample holder. The center mount allows to position the sample inside the integrating sphere. A 100% baseline was established using a measurement with the middle position holder in the integrating sphere and no sample present. Adhesive absorber foils were attached to the back side and surrounding sidewalls of the glass substrate to suppress undesired transmission and stray light, and particularly to avoid reflectance that would otherwise arise from the rear glass interface. The angle-resolved reflectance was then measured by placing the prepared sample into the integrating sphere and the incidence angle was varied by the center mount. For further details on the measurement principles, please refer to the experimental section and to references.<sup>[10,22,23]</sup> As an example, Figure 3b shows reflectance spectra of the rose petal texture measured for angles of incidence  $\theta$  (AOI) from 5° to 80°. The spectra are in agreement with previous reports of rose petals produced on a different material system.<sup>[18]</sup> Further reflectance spectra can be found in Figure S3, Supporting Information.

Figure 4a displays the angle-resolved reflectance (ARR) of representative structures from each class, as determined through experimentation. Each data point corresponds to the average

reflectance within the wavelength range of 330 to 830 nm at a given AOI, with this range selected to exclude absorption lines caused by the glass/resist. The reflectance curves exhibit only a smooth dependency on wavelength, which is why we consider average reflectance values below. For the planar reference, the ARR was both, measured (black symbols in Figure S1, Supporting Information) and calculated with the Fresnel Equations (gray-dashed line); the gray line in Figure 4a shows the arithmetic mean value of  $s$ - and  $p$ -polarized light  $(s + p)/2$  impinging on an air-glass interface. The experimental ARR for a planar glass substrate agrees very well with the theoretical values and validates the experimental setup. Additionally, as anti-reflection coatings (ARCs) are an industry-standard in PV glasses, a single-layer ARC on glass was simulated for the air-to-glass interface with  $n_{\text{ARC}} = \sqrt{n_{\text{glass}}}$  to evaluate the optical properties of the AR textures. The layer thickness of the ARC was set to 123 nm, which is optimized to a quarter of the incident wavelength  $\lambda = 600$  nm and the corresponding refractive index. A comparison of the measured reflectance data of the planar glass with its analytical solution according to Fresnel's equations allows to estimate the error of the reflectance measurements from below 0.1% absolute (near normal incidence) to maximum around 2% absolute (80°). Since the experimental bottom limit in our setup is at  $\theta = 5^\circ$  and the Fresnel Equation shows a very small difference between the reflectance at normal incidence ( $\theta = 0^\circ$ ) and  $\theta = 5^\circ$ , the following reflectance measurements at  $\theta = 5^\circ$  will be addressed as normal incidence for convenience. The reflectance values for the smallest (5°) and largest (80°) AOI for each structure are summarized in the blue columns in Table 1. At moderate angles of incidence, between normal incidence and  $\theta = 55^\circ$ , the planar glass reflects on average 4.5% of the incident light. In comparison, all presented structures in Figure 4a, with one exception (lotus), show highly effective antireflectivity in this angular range. At normal incidence, the strongest antireflective effect is observed for the commercial AR mesotexture, which reduces the reflectance to 0.6%, which is nearly 3.9%<sub>abs.</sub> less than the planar glass reference and maintains the reflectance as low as 3.7% at  $\theta = 55^\circ$ . A comparable performance is observed by the rose petal texture which effectively lowers the reflectance to



**Figure 3.** a) Experimental setup of angle-resolved reflectance measurement inside an integrating sphere using a rotatable center mount. The sample is positioned in the center of the sphere while the incident angle can be adjusted by rotating the sample surface relative to the incident light. Each sample is covered on the back side and sidewalls with a black absorber to block transmission and eliminate reflection from the rear interface. b) Reflectance spectra of rose petal texture measured from 5° to 80° angle of incidence ( $\theta$ ).



**Figure 4.** a) Angle-resolved reflectance spectra of selected structures in which each data point corresponds to the average reflectance between 330 and 830 nm at given  $\theta$ . b) Reflectance at  $\theta = 80^\circ$  as function of surface enhancement factor (SEF) for all textures as indicated.

1.1% and 3.5% at normal incidence and  $\theta = 55^\circ$ , respectively. In the same angular range, the wide-angle diffuser maintains a reflectance from 0.9% to 2.4%. Further, the moth-eye texture, a subwavelength nanotexture, exhibits excellent antireflective properties for moderate AOI,  $\theta < 55^\circ$ , performing best for  $\theta \in [40^\circ, 50^\circ]$ . Random micropyramids perform slightly worse than the aforementioned textures. The only exception is the lotus leaf texture, which shows the smallest antireflectivity, only reducing the reflectance by 1%<sub>abs.</sub> compared to the planar air-glass interface. In comparison, the simulated single-layer ARC on glass exhibits a reflectance of 0.8% at normal incidence, which increases to 1.9% at  $\theta = 55^\circ$ .

For  $\theta > 60^\circ$ , the antireflective behavior of the various textures begins to differ more significantly. The reflectance of planar glass sharply increases from 10% at  $\theta = 60^\circ$  close to 40% at  $\theta = 80^\circ$ . In contrast, the reflectance of micro- and biotextures increases only slightly, keeping the reflectance below 10% until  $\theta = 75^\circ$ . At the largest AOI ( $\theta = 80^\circ$ ), only the reflectance of biotextures and the wide-angle diffuser stay below 10%, with 7.0%, 8.1%, 9.5%, and 9.9% for rose, poinsettia, lotus texture, and wide-angle diffuser, respectively. Interestingly, while the lotus structure hardly reduces reflection for  $\theta < 60^\circ$ , it exhibits a high level of antireflectivity at large incident angles. In contrast, the texture reflecting most at large AOI is the moth-eye structure, whose reflectance increases from 4.8% at  $\theta = 60^\circ$  to 32% at  $\theta = 80^\circ$ , even though it exhibits strong AR performance at low AOI. In comparison, the reflectance of the simulated ARC on glass experiences a very similar increase as the moth-eye structure, in which the reflectance increases from 2.9% at  $\theta = 60^\circ$  to 29.9% at  $\theta = 80^\circ$ . The red-shaded area between the moth-eye structure and the best-performing textures in Figure 4a indicates the significant difference between the antireflective performance at large AOI for the investigated nanostructures and micro-/biotextures. In Figure 4b, we plotted the average reflectance at  $\theta = 80^\circ$  as a function of the SEF. Note the color segregation by the texture classes. Although the mechanisms that cause reduced reflectance differ greatly between texture classes (such as the graded index

effect for subwavelength nanotextures and geometrical ray optics for textures on micro- and mesoscales), there is a general trend that can be observed.<sup>[24]</sup> In the collection of textures investigated in this study, the reflectivity at large AOI ( $\theta = 80^\circ$ ) decreases with increasing SEF. Interestingly, the AR effects of the moth-eye structure can be very effective at low AOI due to the graded index effect, but at large AOI the nanotextures appear to become optically flat, approaching the specular reflectance of a planar surface. In addition, regarding the spectral dependence of reflectance, as illustrated in Figure S3b, Supporting Information, the effectiveness of moth-eye textures also appears to decrease as wavelengths increase. The performance of micro- and biotextures might be explained by ray optical considerations. An enlargement of the surface area is associated with steep flanks at the texture features. The antireflective property arises from multiple reflections of rays on the sidewalls of the features that would be back-reflected if no neighboring features were present. Multiple bounces of the light between adjacent texture features increase the probability to enter the material. As reported by Hünig et al.,<sup>[18]</sup> the excellent performance of the rose petal texture arises from its hierarchically formed surface structure, consisting of a densely packed conical epidermal microtexture, modulated with nanoscale folds. The hierarchical rose petal structure seems to combine the better of two effects: an excellent AR effect for near-normal incident light due to the graded index effect of the nanofolds and great AR capabilities at grazing incidence conditions due to the multiple-reflection effect of the larger features.

### 2.3. Haze and Scattering

After the omnidirectional AR properties of the different textures were analyzed, we determined the angle-resolved scattering profile at normal incidence.<sup>[25]</sup> The angle-resolved scattering profile can provide information about the light path elongation in a solar cell absorber layer, which cannot be obtained from angle-resolved reflectance measurements alone. These

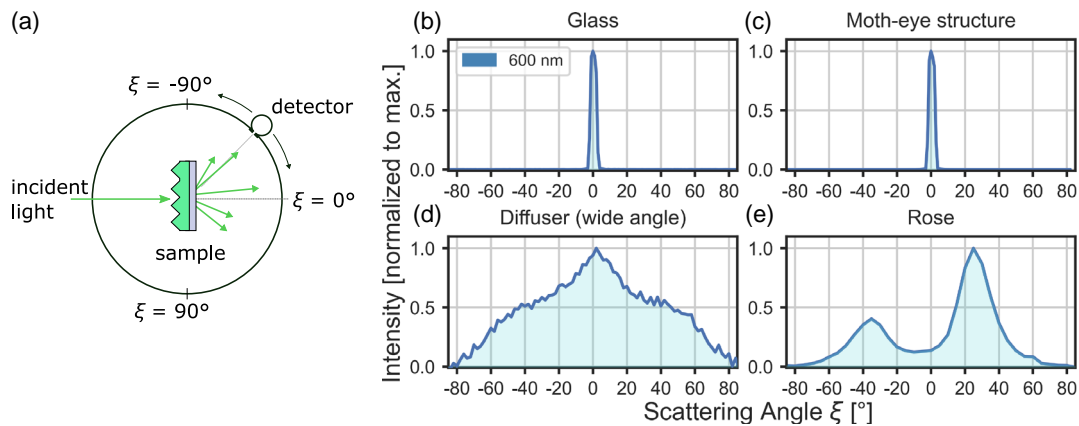


**Figure 5.** a) Automated reflectance/transmittance analyzer (ARTA) instrument configuration illustrating the angle-resolved scatter profile measurement at normal incidence over a narrow range of wavelengths between 590 and 600 nm. The detector is placed in a small integrating sphere that scans the back of the sample to detect scattered light.<sup>[19]</sup> Angle-resolved scatter profile of b) planar glass and three representative textures from c) nanotextures (moth-eye structure), d) artificial microtextures (wide-angle diffuser), and e) biotextures (rose petal) for a wavelength of 600 nm and normalized intensity. The scatter profiles of the other textures are shown in Figure S2, Supporting Information.

measurements only indicate the ability to reduce reflection losses. Angle-resolved scattering profiles were obtained with an automated reflectance/transmittance analyzer (ARTA) in angle-resolved scatter mode.<sup>[26]</sup> The sample is illuminated under normal incidence and the corresponding scattering profile in the transmission is collected for an angular range from  $-85^\circ$  to  $+85^\circ$  (see Figure 5a). The scattering profiles for representative textures of each class (nano, micro, bio) are shown in Figure 5b–e at a single wavelength of 600 nm. For the scattering profiles of the other textures, please see Figure S2, Supporting Information. The scattering profile of planar glass (Figure 5b) peaks at the optical axis ( $\xi = 0^\circ$ ) and is symmetrically confined to  $\xi \in (-10^\circ, 10^\circ)$ , indicating a large share of direct transmittance. The moth-eye structure has an equally narrow scattering profile (Figure 5c), which is representative for the nanotextures. The similarity of the narrow scattering profile suggests that the ability to scatter light is comparable to that of the planar reference. From the class of subwavelength nanotextures even the random nanopyramids show a strong tendency of direct transmittance with 89%. In contrast, the scattering profile of microlens arrays (Figure S2f, Supporting Information) reveals a wide scattering profile, with two peaks formed symmetrically at  $\xi = \pm 35^\circ$  and a significantly reduced direct transmittance at  $\xi = 0^\circ$ . The widest scattering profile for all samples is found for the wide-angle diffuser (Figure 5d), which shows a characteristic peak at  $\xi = 0^\circ$ , still, a very large portion of the total intensity is scattered into a large angular range. Furthermore, the rose petal texture (Figure 5e) also scatters into two distinct asymmetric peaks. The dominant peak is located around  $\xi = +24^\circ$ , while a less pronounced peak is at  $\xi = -35^\circ$ . In addition, we calculated the directional transmittance between  $\xi = \pm 12.5^\circ$  from the scattering profiles and expressed as a percentage of the total intensity (see Table 1). The angular range is set according to the detector slit opening angle used here. As expected, the directional transmittance for both, the planar glass and the moth-eye structure is equal to 99.9%. For the rose-petal texture, however, only 7% of the incident light is transmitted between  $\xi = \pm 12.5^\circ$ , which is

notably less than for comparable bioinspired textures with 34.4% and 53.7% for the lotus and poinsettia textures, respectively. The scattering profiles of the lotus and poinsettia textures (Figure S2g,h, Supporting Information) have a large peak at the center of the optical axis ( $\xi = 0^\circ$ ). For the poinsettia texture, we observe a larger broadening and consequently a smaller directional transmittance. Additionally, the microlens array and the random micropylamid texture both strongly redirect the light away from the optical axis, amounting to 11.7% and 22.4% directional transmittance, respectively. The random micropylamid shows two symmetrically shaped scattering peaks (Figure S2d, Supporting Information) at  $\xi = \pm 21^\circ$ , a characteristic angle, which has been reported earlier.<sup>[27,28]</sup> At last, for the wide-angle diffuser a significant share of 31.7% of the total intensity amounts to directional transmittance. The directional transmittance may be interpreted such that a reduction of light intensity around the optical axis is caused by the scattering of the in-coupled light into larger propagation angles. In literature, such broadening of scattering angles was often associated with light path enhancement and light trapping effects that increased the absorption probability of the underlying absorber material.<sup>[8,10,29,30]</sup> As Li et al. have shown by simulations, silicon absorbers illuminated under an AOI of  $\theta = 80^\circ$  and equipped with rose-textured foils were able to preserve an absorption level close to normal incidence. Besides, the antireflective effect, light trapping was reported to be another substantial effect increasing solar cell performance.<sup>[31]</sup> In contrast, similar attributes can be expected to be at a very small level for the nanotextures. In this regard, the moth-eye structure, despite showing a significant degree of antireflectivity at low angles of incidence, could be therefore inferior to large-scale structures when used as an external light management texture, due to the absence of light path enhancing and light trapping potential. Please note that in this experimental setup, a part of the light might scatter to larger angles, experiencing total internal reflection at the rear side of the glass. This part of the light is not detected in these measurements.

Next, to quantify the totally scattered light in all three dimensions, we analyzed the haze in transmission, which is the ratio of diffuse and total transmittance.

$$H_T = \frac{T_{\text{diff}}}{T_{\text{tot}}} \quad (1)$$

The haze and the angle-resolved scattering profile are closely related parameters, with the difference, that the angular information along the measurement axis is preserved in the scatter profiles, while the haze accounts for the total integrated photon flux deviating outside the  $2.5^\circ$  escape cone of forward transmitted light.<sup>[32]</sup> The haze from 330 to 1,200 nm is depicted in **Figure 6a** and summarized in Table 1. It is striking that large-scale micro- and biotextures have haze close to unity. Notably, the random micropyramids show a slight drop of haze starting from 800 nm to longer wavelengths, which might be due to feature sizes becoming comparable to the wavelength.<sup>[8]</sup> In contrast, the planar glass shows zero haze, and the moth-eye structure only scatters weakly at a short wavelength comparable to its feature size. As shown in **Figure 6b**, for the collection of textures investigated in this study, we observe a correlation between averaged haze factor and the structure properties, expressed by the SEF. While most nanotextures with small SEF exhibit little to no light scattering ability, with increasing SEF, higher scattering haze factors are observed. As already visualized by the scattering profiles, broad geometrical scattering becomes dominant for large-scale textures.

## 2.4. Energy Yield Analysis

Based on the experimental ARR results, we analyze the effect of the textured PV glass on the potential energy yield of PV modules using simulations. To investigate, how textures affect the energy yield of PV modules, we calculate the time-integrated irradiance, also known as radiant exposure  $H$ , on a bifacial PV module in Berlin, Germany (**Figure 7a**). As source for the meteorological irradiance, we use hourly data for 2005–2019 provided by the

Copernicus Atmosphere Monitoring Service.<sup>[33]</sup> The irradiance on the front and back sides of PV modules is calculated with in-house developed software. This detailed illumination model considers shading and reflections from the ground for a large periodic array of PV modules rows (**Figure 7b**). The details of the illumination model are described in the study of Jäger et al.<sup>[34]</sup> For this work, we extended the model to extract the incident angle of the irradiance on the PV module front and back side in terms of the polar angle  $\theta$  and azimuth  $\varphi$ , with respect to the module surface. Note, that the polar angle is equivalent to the angle of incidence discussed earlier.

To calculate the fraction of the radiant exposure  $H_{\text{inc}}$ , which is coupled into the PV module, we have to weight with the angle-dependent reflectivity  $R(\theta)$  of the respective surface texture

$$H_{\text{inc}} = \int_0^{2\pi} \int_0^\pi \bar{\Lambda}(\theta, \varphi) (1 - R(\theta)) \sin\theta \, d\theta \, d\varphi \quad (2)$$

Here,  $\bar{\Lambda}$  denotes the mean annual angle-resolved radiant exposure, which is given by

$$\bar{\Lambda}(\theta, \varphi) = \frac{1}{T} \int_0^T L(t, \theta, \varphi) \cos\theta \, dt \quad (3)$$

with the radiance  $L$  and the duration  $T$  for which data are available (in years, here 2005–2019).

An advantage of using simulations is that experimentally acquired ARR data can be flexibly transferred to different exposure scenarios. For this study,  $\bar{\Lambda}$  was calculated for a bifacial PV module with optimal tilting angle  $\beta$  (in terms of maximized total radiant exposure onto the back and front sides), which is  $\beta = 37^\circ$  for a module facing south in Berlin, Germany (**Figure 7a**). The following discussion is focused on this bifacial configuration with optimal tilt, for five different surfaces on the glass cover. We assumed a module length  $\ell = 1.96$  m, module height  $h = 0.5$  m, spacing between module rows of 6 m, and a ground albedo of 30%. **Figure 7c,d** shows  $\bar{\Lambda}$  calculated for the front and back sides of the bifacial configuration with optimal tilt. In each polar plot, the coordinates at the outermost circle refer to the

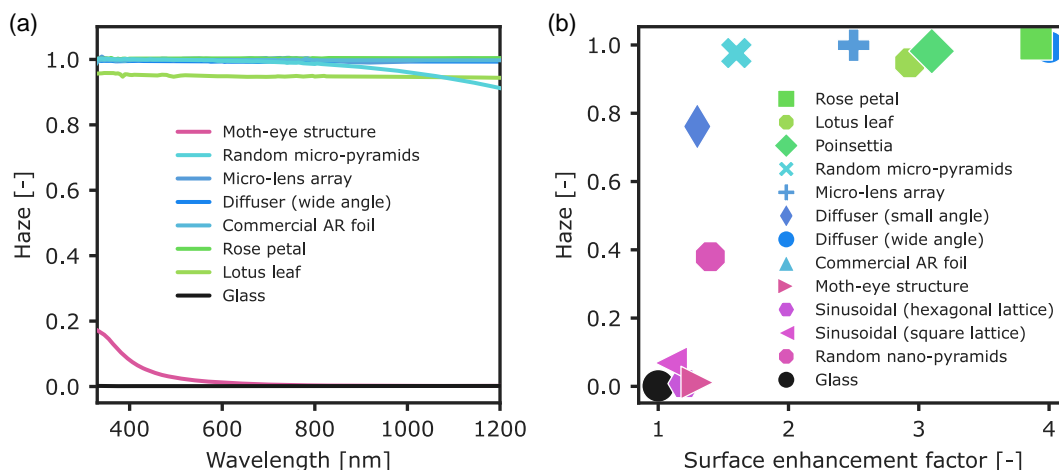


**Figure 6.** a) Haze measurement of selected structures. Planar glass exhibits zero diffuse transmittance, whereas large-scale micro- and biotextures show large scattering power, as close as unity over the entire bandwidth. b) Average haze factor in the regime from 330 nm to 1,200 nm as function of surface enhancement factor.

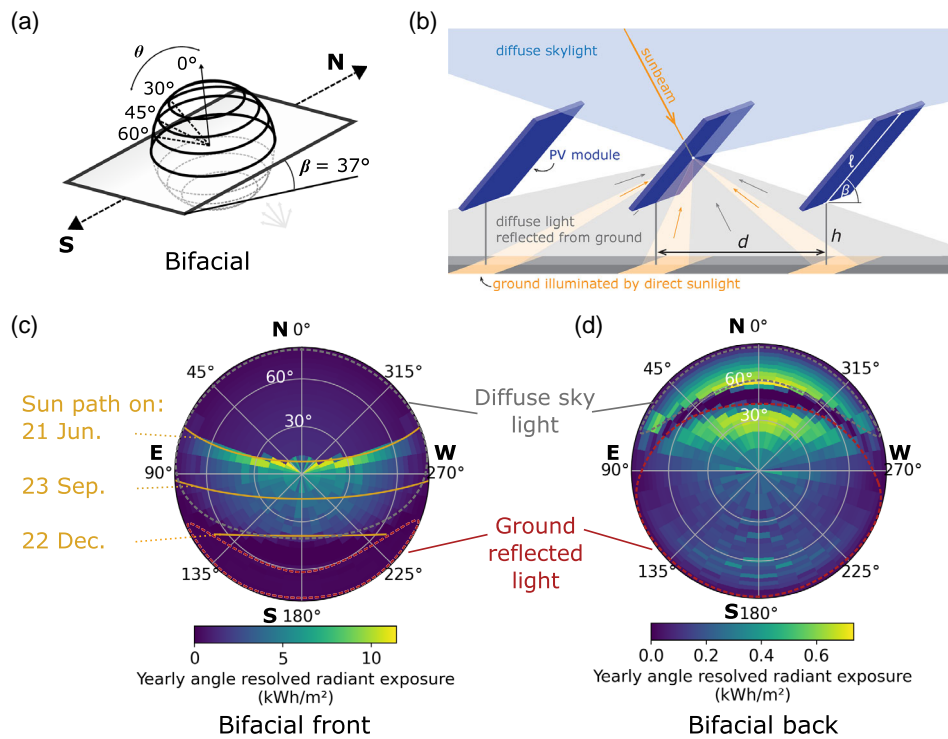


**Figure 7.** a) Schematic illustrations of PV module setups for energy yield calculation for a bifacial module with optimal tilt for Berlin, Germany, facing south. b) Schematic illustration of bifacial irradiance model and input parameters upon which the calculation is based. Reproduced with permission under the terms of the Creative Commons CC BY license.<sup>[35]</sup> Copyright 2021, the Authors. Published by Wiley-VCH. c, d) Corresponding mean annual angle-resolved radiant exposure  $\bar{\Lambda}$  for c) front and d) back side of bifacial module with optimal tilt. The orange lines indicate the path of the sun over the module on 21 June (midsummer), 23 September (equinox), and 22 December (winter solstice), between which direct sunlight can be received throughout the year. The dashed gray and red lines mark the diffuse skylight and ground-reflected light, respectively.

azimuth  $\varphi$  in the module plane of each module side. In Figure 7c for the module front side,  $0^\circ$  corresponds to the north,  $270^\circ$  to the west,  $180^\circ$  to the south, and  $90^\circ$  to the east. For the module rear side (Figure 7d), the relative azimuth changes, with  $90^\circ$  and  $270^\circ$  corresponding to west and east, respectively. At the center/origin of the polar coordinates is the surface normal of the module, hence, corresponding to the tilt angle  $\beta$  of the module. In other words, for the front side, the observer is looking from the module toward the sky, looking upright at a  $37^\circ$  tilt. Whereas for the back side, the observer is looking from the module toward the ground. The angle-resolved radiant exposure  $\bar{\Lambda}$  on the front side consists of three main components. First, the diffuse light from the sky is received from the section that is limited by the gray-dashed line. The orange lines mark the path of the sun on 21 June (summer solstice), 23 September (equinox), and 21 December (winter solstice) over the module. Between these lines, direct sunlight can be received throughout the year. Because winter days are often cloudy in Berlin, direct sunlight mainly hits the module during spring and summer. Hence, the brightest areas are concentrated along the sun's path during summer. At the bottom of the hemisphere, low intensity of light is received from ground reflection, indicated by the section limited with a dark red-dashed line. For the back side (Figure 7d), the majority of the hemisphere is covered by the section of ground-reflected light, which is the largest contribution to the back-side illumination. At the top, the small section limited by the gray dashed line shows illumination from

diffuse skylight, while the dark area between the diffuse skylight and the ground reflection is composed of the blocked view from the next row behind the investigated module. Note that the color scales for the front and back sides differ by about one order of magnitude.

Figure 8 and S5, Supporting Information, show the in-coupled ( $H_{inc}[\theta]$  and reflected) radiant exposures at the front and back sides for five different surfaces, which reach the module in a polar angle interval  $[\theta - \Delta/2, \theta + \Delta/2]$ , where  $\Delta$  is the length of the interval. The total radiant exposures at the front and back sides of the module ( $1,179$  and  $160 \text{ kWh m}^{-2} \text{ year}^{-1}$ , respectively) are constant for all scenarios. At the front, around 85% of the incident light reaches the module for  $\theta \in [15^\circ, 55^\circ]$ . Only 10% of the radiant exposure comes from  $\theta > 60^\circ$ . At the rear side of the module, 45% of the incident light reaches the module for  $\theta \in [60^\circ, 80^\circ]$ . The ratio of in-coupled to reflected radiant exposure depends on the angle-dependent surface reflectivity of the textures and coating, which we assume to be at both the front and back sides of the module. Figure S5, Supporting Information shows the results for a module with a planar cover glass where we observe significant reflection losses in the entire angular range amounting to 6.6% in total composed of a loss of 6.0% and 10.5% for the front and back side, respectively (Table 2).

Figure 8a depicts the results for a module with an ARC on glass, which effectively reduces the total reflection losses in

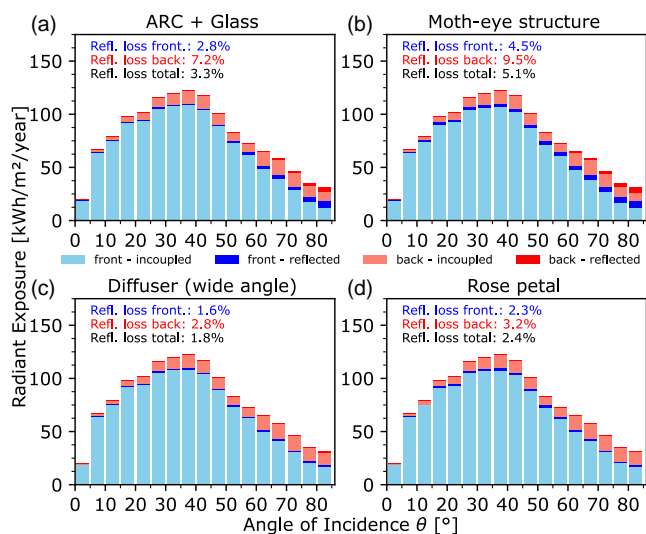


**Figure 8.** In-coupled ( $H_{inc}[\theta]$  and reflected) radiant exposures at the front and back sides, for light that reaches the module in a polar angle interval  $[\theta - \Delta/2, \theta + \Delta/2]$  on a module glass with a) an ARC coating, b) a moth-eye structure, c) a diffuser (wide angle), and d) a rose petal texture.  $\Delta$  is the length of the angle interval, here  $\Delta = 5^\circ$ . The total incident radiant exposure (in-coupled + reflected) is independent of the texture. The cumulative relative reflected losses with respect to the front, back and total radiant exposure are given in each graph. The darker hue bars indicate the proportion of the total radiant exposure that is reflected. The calculation is based on the averaged surface reflectivity between 420 and 1,150 nm (cf. Table 1).

the entire angular range to 3.3%, with a loss of 2.8% for the front side and 7.2% for the back side. For a moth-eye structured resist on glass (Figure 8b), very low reflection losses are shown at angles of incidence  $\theta < 55^\circ$ , originating from the strong antireflective properties of this nanotexture. We observe that the reflection losses at the front are reduced by almost a factor of two, when compared to the planar surface. However, previously discussed shortcomings of the investigated moth-eye structure are visible at large AOI  $\theta > 60^\circ$ , where the reflection losses increase significantly. The total reflected loss of 3.6% for a bifacially operated module is composed of 3.1% and 7.2% loss for the front and back side, respectively. In Figure 8c,d, both, wide-angle diffuser and rose texture, enhance light in-coupling by reducing front-side reflection losses to 1.6% and 2.3%, respectively. In total, the rose petal and the wide-angle diffuser achieve the highest annual reduction of reflection losses from 6.6% (planar glass) to 2.2% and 1.8%, respectively, resulting in an enhanced energy yield of 4.7% and 5.1%. Benchmarking the performance of both

textures on the ARC on glass, the total energy yield is increased by 1.5% and 1%, respectively. Interestingly, the advantages of these large-scale microtextures and hierarchical biotextures come into play, especially, on the back side. The relative gain of in-coupled light at the module back side with either texture substantially increases up to 9%<sub>rel.</sub>, when compared to a planar back side, due to the exceptionally low reflectance at  $\theta > 60^\circ$ . Also, compared to the ARC on glass, the back side efficacy of light in-coupling can be enhanced by the best-performing textures by approximately 5%.

In an alternative approach, the share of light impinging at shallow angles can be substantially reduced by using a single-axis tracking system. Therefore, we regard omnidirectional textures as investigated in this study, particularly, important for fixed PV systems with nonoptimum orientation (such as in BIPV or vertical PV) or with a high share of diffuse illumination (such as in bifacial PV).

Finally, we estimated the potential impact of front glass panel textures on solar cell performance by laminating the resist textured glasses on silicon solar cells and measuring current-voltage characteristics at different angles of incidence. The current density was found to increase by about 1%–4% (relative) for normal incidence illumination and about 6%–7% (relative) for illumination at  $60^\circ$  when replacing a planar glass panel with glasses featuring micropylamidal or rose petal textures (see Figure S4 and Table S2, Supporting Information).

### 3. Conclusion

In this work, we used UV nanoimprint lithography to fabricate 12 different textures at nano- and microscales, as well as bio-inspired textures on resist-coated glass. This enabled us to characterize the angle-dependent optical performance of textures while keeping the material system identical. Further, we not only studied reflectance at normal incidence, but for a wide angular range. This is important, because the surface reflectivity varies substantially for different textures for angles of incidence (AOI)  $\theta > 60^\circ$ . We found that the samples with large textures, which are in the geometrical scattering regime, have superior antireflective properties at large AOI compared to subwavelength textures, and can offer effective broadband, omnidirectional antireflection. We further observed a correlation between large surface enhancement factor and low reflectance at  $\theta = 80^\circ$ . As best performing omnidirectional antireflective textures we identified a bioreplicated rose petal texture and a wide-angle diffuser microtexture, with reflectance values of 1.2% and 0.8% at normal incidence, and 6.5% and 9.3% at  $\theta = 80^\circ$ , respectively. This performance translates to increased current-voltage characteristics

**Table 2.** Total radiant exposure and relative reflected radiant exposure for bifacial PV modules with four selected surfaces for Berlin, Germany. The module is facing south, with an optimal module tilt of  $37^\circ$ , 1.96 m module length, and 0.5 m height above the ground. For the ground, a 30% albedo is assumed.

Radiant exposure total [ $\text{kWh m}^{-2} \text{year}^{-1}$ ]			Relative reflected radiant exposure [%]											
			ARC on Glass			Moth-eye structure			Diffuser (wide angle)			Rose petal		
Front	Back	Total	Front	Back	Total	Front	Back	Total	Front	Back	Total	Front	Back	Total
1,174	160	1,335	2.8	7.2	3.3	4.5	9.5	5.1	1.6	2.8	1.8	2.3	3.2	2.4

under varying incident angles. Further, we investigated the potential impact of surface texturing on the energy yield of bifacial solar modules, assuming optical gains translate directly to the electrical yield. For this, the in-coupled and reflected light was simulated using calculated angle resolved annual radiant exposure and surface reflectivity of the front and back sides according to our experimental data. When compared to a planar reference, the rose petal and the wide-angle diffuser provided the greatest increase in annual yield of 4.7% and 5.1%, respectively. When comparing the performance of the two textures with a single-layer antireflection coating on glass, it was found that they increased the total energy yield by 1% and 1.5%, respectively. We discovered that particularly the back side of the bifacial module benefits from an omnidirectional anti-reflective texture, as a large fraction of the incident light impinges at large AOI. These calculations did not consider light-trapping effects. Hence, the real energy yield gain might be even higher. The results underline the importance of omnidirectional antireflective textures, particularly, in the emerging fields of bifacial, vertical, and building-integrated PV with a high share of sunlight impinging at shallow angles.

#### 4. Experimental Section

**Processing:** In this work, 12 different textures from the nano-, micro-, and mesoscales were investigated and compared to a planar reference. The original (master) structures were both of artificial and natural origin. All textures were processed by UV-nanoimprint lithography (UV-NIL) using the UV-curable NIL-resist OrmoComp (microresist technology) on glass substrates (Schott, D263 T eco) with a 1.1 mm gauge. For the artificial master structures, viscous polydimethylsiloxane (PDMS, Wacker) was cast on the master and cured at 70 °C for 20 min to replicate a negative of the template. The NIL resist was then deposited on the glass substrate by spincoating for 30 s at 3,000 rpm. For spincoating, the NIL-resist was either used nondiluted or diluted with the solvent OrmoThin (microresist technology) in different mass ratios ranging between 3:1, 1:1, and 1:3 to match adequate layer thicknesses, corresponding to the respective vertical structural dimensions. Diluted resists were soft-baked for 2 min at 80 °C. The PDMS negative was then gently applied to the soft-baked resist and UV illuminated for 5 min. To avoid damaging the delicate surfaces, the processing steps for biotextures were modified by casting PDMS onto fresh petals and leaves and curing them at 40 °C for 4 h. Nondiluted OrmoComp was dropcasted to the glass substrate and evenly distributed to a layer thickness of approximately 2 mm using a self-made blade coater. The cured PDMS stamp was then carefully applied to the resist and illuminated for 10 min; a detailed description of the UV-NIL process of biotextures can be found in the study of Yoo et al.<sup>[21]</sup> After the UV exposure, the AR structures were hard-baked for 3 h at 180 °C to improve the refractive index and bring it closer to that of the glass substrate. For optical characterization, the structures were processed on 2.5 × 5 cm<sup>2</sup> glass substrates.

**Surface Imaging:** The surface topography of all processed textures was imaged, depending on their scale, by means of scanning electron microscopy (Zeiss), atomic force microscopy (XE-70 & NX12, Park Systems) in noncontact mode, and a confocal laser scanning microscopy (VK-X260 & VK-X3000, Keyence). The latter two methods were used to determine the structural parameters by using the software analysis tools Gwyddion and MultiFileAnalyzer (Keyence).

**Optical Measurements:** Hemispheric total transmittance, diffuse transmittance, and angle-resolved reflectance measurements were carried out on a Perkin Elmer Lambda 1050 + UV-vis-NIR spectrophotometer, equipped with a photo-multiplier-tube and an indium gallium arsenide detector. The latter was measured by attaching the samples to an angle

variable center mount, which allows sample positioning in the center of the integrating sphere. Reflectance spectra were recorded with increasing angles of incidence from 5° to 80° in 5° steps. The back side of the glass substrate was covered with a black absorber film (d-c-fix, uni) to suppress reflection from the back glass-air interface. The substrate edges were optically blocked by using a black pen (Edding) to minimize the light-outcoupling at the edges. For the measurement of the angle-resolved scattering, the spectrophotometer was expanded with a modular automated reflectance/transmittance analyzer (ARTA) setup. The transmittance of the samples was measured at various angles and wavelengths using a detector on a motorized goniometric stage. The stage scanned from +85° to −85° on the horizontal axis around the sample.

#### Supporting Information

Supporting Information is available from the Wiley Online Library or from the author.

#### Acknowledgements

The authors thank the Helmholtz Einstein International Berlin Research School in Data Science (HEIBRIDS) and the Deutsche Bundesstiftung Umwelt (DBU, grant no. 37908/01) for partial funding of the project. The authors also thank Mark Khenkin and Quiterie Emery from Helmholtz-Zentrum Berlin for providing the encapsulated solar cells. Temicon acknowledges financial support from the German Ministry for Economic Affairs and Climate Action through the project Vorfahrt (FKZ 03EE1142A).

Open Access funding enabled and organized by Projekt DEAL.

#### Conflict of Interest

The authors declare no conflict of interest.

#### Data Availability Statement

The data that support the findings of this study are available from the corresponding author upon reasonable request.

#### Keywords

energy yield calculations, nanoimprint lithography, omnidirectional antireflective textures, photovoltaics

Received: January 31, 2023

Revised: May 11, 2023

Published online: May 28, 2023

- [1] J. A. Dobrowolski, D. Poitras, P. Ma, H. Vakil, M. Acree, *Appl. Opt.* **2002**, *41*, 3075.
- [2] VDMA, International Roadmap for Photovoltaic (ITRPV), [itrpv.vdma.org](http://itrpv.vdma.org), (accessed: September 2022).
- [3] D. Chen, *Sol. Energy Mater. Sol. Cells* **2001**, *68*, 313.
- [4] B. G. Priyadarshini, A. K. Sharma, *Bull. Mater. Sci.* **2016**, *39*, 683.
- [5] C. L. Pinto, I. Cornago, A. Buceta, E. Zugasti, J. Bengochea, *Sol. Energy Mater. Sol. Cells* **2022**, *246*, 111935.
- [6] J. Cai, L. Qi, *Mater. Horiz.* **2015**, *2*, 37.
- [7] M. Jošt, S. Albrecht, L. Kegelmann, C. M. Wolff, F. Lang, B. Lipovšek, J. Krč, L. Korte, D. Neher, B. Rech, M. Topič, *ACS Photonics* **2017**, *4*, 1232.

- [8] D. Eisenhauer, C. T. Trinh, D. Amkreutz, C. Becker, *Sol. Energy Mater. Sol. Cells* **2019**, *200*, 109928.
- [9] S. J. Choi, S. Y. Huh, *Macromol. Rapid Commun.* **2010**, *31*, 539.
- [10] R. Schmager, B. Fritz, R. Hünig, K. Ding, U. Lemmer, B. S. Richards, G. Gomard, U. W. Paetzold, *ACS Photonics* **2017**, *4*, 2687.
- [11] U. Blieske, T. Doege, P. Gayout, M. Neander, D. Neumann, A. Prat, in *3rd World Conf. on Photovoltaic Energy Conversion*, IEEE, Osaka, **2003**.
- [12] W. A. Nositschka, D. Neumann, in *23rd European Photovoltaic Solar Energy Conf. and Exhibition*, WIP, Valencia, **2008**.
- [13] C. Ulbrich, G. Andreas, K. Hermans, A. Lambert, U. Rau, *Prog. Photovoltaics* **2013**, *21*, 1672.
- [14] temicon GmbH, Microlens Array Molds by Interference Lithography IL-MLA, <https://www.temicon.com/technologies/nano-and-micro-structures/micro-lens-arrays> (accessed: January 2023).
- [15] A. Harter, S. Mariotti, L. Korte, R. Schlatmann, S. Albrecht, B. Stannowski, *Prog. Photovoltaics* **2023**, <https://doi.org/10.1002/pip.3685>.
- [16] temicon GmbH, Holographic Surface Diffusers Flyer, <https://www.temicon.com/technologies/nano-and-micro-structures/diffusers>, (accessed: January 2023).
- [17] S. Choo, H.-J. Choi, H. Lee, *Mater. Lett.* **2014**, *121*, 170.
- [18] R. Hünig, A. Mertens, M. Stephan, A. Schulz, B. Richter, M. Hetterich, M. Powalla, U. Lemmer, A. Colsmann, G. Gomard, *Adv. Opt. Mater.* **2016**, *4*, 1487.
- [19] W. Barthlott, C. Neinhuis, *Planta* **1997**, *202*, 1.
- [20] S. Dai, D. Zhang, Q. Shi, X. Han, S. Wang, Z. Du, *CrystEngComm* **2013**, *15*, 5417.
- [21] D. Yoo, S. Garud, C. T. Trinh, D. Amkreutz, C. Becker, *IEEE J. Photovoltaics* **2021**, *12*, 97.
- [22] I. Haedrich, M. Ernst, A. Thomson, P. Zheng, X. Zhang, H. Jin, D. Macdonald, *Sol. Energy Mater. Sol. Cells* **2018**, *183*, 181.
- [23] P. Maddalena, P. Tortora, A. Parretta, in *19th Congress of the Inter. Commission for Optics: Optics for the Quality of Life*, SPIE, Firenze, Italy, **2002**.
- [24] H. K. Raut, V. A. Ganesh, A. S. Nair, S. Ramakrishna, *Energy Environ. Sci.* **2011**, *4*, 3779.
- [25] K. Jäger, O. Isabella, R. van Swaaij, M. Zeman, *Meas. Sci. Technol.* **2011**, *22*, 105601.
- [26] P. A. van Nijnatten, *Thin Solid Films* **2003**, *442*, 74.
- [27] T. E. Scheul, E. Khorani, T. Rahman, M. D. B. Charlton, S. A. Boden, *Prog. Photovoltaics* **2020**, *28*, 1248.
- [28] E. Forniés, C. Zaldo, J. M. Albella, *Sol. Energy Mater. Sol. Cells* **2005**, *87*, 583.
- [29] A. Roslizar, S. Dottermusch, R. Schmager, M. Guttman, G. Gomard, H. Hölscher, B. S. Richards, U. W. Paetzold, *Sol. Energy Mater. Sol. Cells* **2020**, *214*, 110582.
- [30] B. Zheng, W. Wang, G. Jiang, X. Mei, *Appl. Phys. B* **2016**, *122*, 180.
- [31] K. Li, R. Wu, Y. Ruan, L. Zhang, H. Zhen, *Sol. Energy* **2018**, *170*, 800.
- [32] F. W. Billmeyer, Y. Chen, *Color Res. Appl.* **1985**, *10*, 219.
- [33] Z. Qu, A. Oumbe, P. Blanc, B. Espinar, G. Gesell, B. Gschwind, L. Klüser, M. Lefèvre, L. Saboret, M. Schroedter-Homscheidt, L. Wald, *Meteorol. Z.* **2017**, *26*, 33.
- [34] K. Jäger, P. Tillmann, C. Becker, *Opt. Express* **2020**, *28*, 4751.
- [35] K. Jäger, P. Tillmann, E. A. Katz, C. Becker, *Sol. RRL* **2021**, *5*, 2000628.